SOFT ROBOTS

Soft robot–mediated autonomous adaptation to fibrotic capsule formation for improved drug delivery

Rachel Beatty[1,2]†, Keegan L. Mendez[3,4]†, Lucien H. J. Schreiber[1]†, Ruth Tarpey[1,5,6], William Whyte[4], Yiling Fan[7], Scott T. Robinson[1,2], Joanne O'Dwyer[1], Andrew J. Simpkin[8], Joseph Tannian[1], Peter Dockery[1], Eimear B. Dolan[1,5,6], Ellen T. Roche[3,4,7]*, Garry P. Duffy[1,2,5]*

The foreign body response impedes the function and longevity of implantable drug delivery devices. As a dense fibrotic capsule forms, integration of the device with the host tissue becomes compromised, ultimately resulting in device seclusion and treatment failure. We present FibroSensing Dynamic Soft Reservoir (FSDSR), an implantable drug delivery device capable of monitoring fibrotic capsule formation and overcoming its effects via soft robotic actuations. Occlusion of the FSDSR porous membrane was monitored over 7 days in a rodent model using electrochemical impedance spectroscopy. The electrical resistance of the fibrotic capsule correlated to its increase in thickness and volume. Our FibroSensing membrane showed great sensitivity in detecting changes at the abiotic/biotic interface, such as collagen deposition and myofibroblast proliferation. The potential of the FSDSR to overcome fibrotic capsule formation and maintain constant drug dosing over time was demonstrated in silico and in vitro. Controlled closed loop release of methylene blue into agarose gels (with a comparable fold change in permeability relating to 7 and 28 days in vivo) was achieved by adjusting the magnitude and frequency of pneumatic actuations after impedance measurements by the FibroSensing membrane. By sensing fibrotic capsule formation in vivo, the FSDSR will be capable of probing and adapting to the foreign body response through dynamic actuation changes. Informed by real-time sensor signals, this device offers the potential for long-term efficacy and sustained drug dosing, even in the setting of fibrotic capsule formation.

INTRODUCTION

A critical hurdle associated with long-term implantable medical devices is the foreign body response (*1*). The foreign body response is a highly complex process that includes inflammation, proliferation, and tissue remodeling (*2*–*4*). Innate immune cells are rapidly recruited to the implant site to engulf the foreign material (*3*, *5*, *6*). Because of the device's continued presence (*7*, *8*), chronic inflammation occurs, resulting in the recruitment of inflammatory cells (*9*). Myofibroblasts lay down a layer of collagen around the implanted material, causing fibrotic encapsulation (*1*). Collagen deposition stops the device from interacting with surrounding tissues (*8*), often leading to device impairment and failure. The foreign body response is the single largest hurdle to unlocking the clinical potential of implantable drug delivery and biosensing devices, because they rely on direct communication with the surrounding tissue.

Several strategies that focus on modifying or overcoming this response have emerged recently, including implant surface; size and shape modifications; the delivery of modifying agents, including anti-fibrotic and anti-inflammatory drugs; and the use of biomimetic materials (*3*, *10*–*14*). These approaches have been met with mixed success. Implant modifications have primarily been designed to tackle one specific aspect of the foreign body response and therefore fail to address its complexity. Moreover, being able to adjust dosing on the basis of its temporal heterogeneity (because implant size/shape cannot be adjusted) has not yet been explored. Although delivery of fibrotic-modifying agents may exhibit temporary blunting of the immune response, there remain concerns about local toxicity and off-target adverse effects, and sustained, systemic delivery of such is associated with liver, kidney, cardiac, and gastrointestinal toxicities (*15*, *16*). A long-term, drug-free solution that could modify the foreign body response, while also adapting to its changes over time, would address many of these limitations. Mechanotherapy is one such emerging concept, which aims to improve implant function by altering the material's surrounding environment via mechanical actuation. For example, extrinsic magnetic actuators were used to reduce capsular development in implantable ferrogel scaffolds (*17*). Soft robotics represents a particularly useful technology in this context, with the potential to gently and minimally invasively interact with soft tissues. Our laboratory has already shown the ability to alter biomechanical properties at an implant site by reducing fibrotic capsule formation using intermittent soft robotic actuation (*1*, *18*). We recently demonstrated that such mechanotherapy significantly improved drug delivery, resulting in near-complete preservation of implanted device–mediated drug delivery in a mouse model over an 8-week period (*18*). This technique can also increase mass transport and therapeutic effect via on-demand actuations that enable rapid release of a large bolus of drug, even in the presence of the fibrotic capsule (*18*). However, these strategies are largely unguided, using a predetermined actuation regimen, which does not account for patient or

[1]Anatomy and Regenerative Medicine Institute (REMEDI), School of Medicine, University of Galway, Galway, Ireland. [2]SFI Centre for Advanced Materials and BioEngineering Research (AMBER), Trinity College Dublin, Dublin, Ireland. [3]Harvard-MIT Program in Health Sciences and Technology, Cambridge, MA, USA. [4]Institute for Medical Engineering and Science, Massachusetts Institute of Technology, Cambridge, MA, USA. [5]CÚRAM, Centre for Research in Medical Devices, University of Galway, Galway, Ireland. [6]Biomedical Engineering, School of Engineering, University of Galway, Galway, Ireland. [7]Department of Mechanical Engineering, Massachusetts Institute of Technology, Cambridge, MA, USA. [8]School of Mathematical and Statistical Sciences, University of Galway, Galway, Ireland.
*Corresponding author. Email: etr@mit.edu (E.T.R.); garry.duffy@universityofgalway.ie (G.P.D.)
†These authors contributed equally to this work.

implant site variability or the progressive nature of the foreign body response. Furthermore, these studies report notable heterogeneity with respect to actuation regimen, including frequency, duration, and level of device deformation or tissue strain (*17*, *19*–*22*). Consequently, little is understood about the optimal loading parameters that maximize the anti-fibrotic effects of mechanical actuation. Although we have demonstrated that actuation can be used for enhanced drug delivery, we had no means to tailor the actuation regimen to individual patients. Moreover, for devices intended for long periods of implantation and/or particularly sensitive tasks, such as releasing small amounts of insulin in response to slight changes in blood glucose levels, monitoring and adjusting device function is crucial for long-term success. If the foreign body response could be monitored in real time by sensing in situ physiological signals, this information could be harnessed in a feedback system to inform the actuation regimen and precisely deliver a consistent drug dose, regardless of the level of fibrosis. Machine learning and artificial intelligence, informed by patient-specific physiological signals, could be leveraged to offer personalized treatment for individual fibrotic capsules. The ability to slow capsular formation, while also sustaining and controlling drug delivery over time by increasing the magnitude and number of actuations, could result in improved device longevity and overall implant function.

Here, we present the FibroSensing Dynamic Soft Reservoir (FSDSR) (Fig. 1A), a biocompatible soft robotic drug delivery device capable of monitoring the foreign body response in vivo via in situ sensing of physiological signals related to fibrotic capsule formation. This study focuses on the development and incorporation of a fibrotic sensing (FibroSensing) membrane into this drug delivery device. Pressure to the actuatable reservoir compresses the inner therapeutic reservoir to release drug (Fig. 1B and movies S1 and S2) (*1*, *18*). The FSDSR (Fig. 1C and fig. S1, C and D) advances substantially on previous iterations of our mechanotherapeutic implant (*18*) by using the principles of electrochemical impedance spectroscopy to quantify fibrotic capsule formation and the resulting degree of porous membrane occlusion. Electrochemical impedance spectroscopy is a noninvasive technique used to characterize electrical properties of materials (*23*, *24*) through impedance (Z), which measures the opposition to electrical movement in a system (*23*). It has been used to study biological tissues in ex vivo and in vivo environments (*25*–*30*). By developing a porous membrane capable of conducting an electrical signal, we propose that the foreign body response can be monitored in real time by analyzing changes in the electrical impedance. By providing feedback to the device, informed by machine learning, we could tune the mechanotherapeutic regimen to ensure consistent drug release over time, regardless of fibrotic encapsulation (Fig. 1D). Although we show one design of the FSDSR, it is a highly versatile platform that could be manufactured in a variety of configurations for diverse applications. To date, an implantable device that can sense, respond to, and overcome the foreign body response–mediated drug diffusion barrier in real time has not yet been realized, and such capabilities could greatly enhance the clinical potential of implantable medical technologies.

RESULTS

Fabrication and characterization of the FSDSR

The size and shape of the FSDSR are easily customizable because of the use of thermoplastic polyurethane (TPU), the three-dimensional (3D) molding, and the thermoforming processes. TPU is widely used in the medical industry because of its excellent mechanical properties and durability (*31*, *32*). It can be easily processed and shaped (thermoplastic properties) while also maintaining excellent elasticity (elastomeric properties). Medical-grade formulations, such as aliphatic and aromatic TPUs, have also been developed for long-term implantation applications that show improved oxidative and biocompatibility properties. The pore pattern and density (fig. S1A) of the TPU membrane can also be changed depending on device requirements. A low-density pattern (100-μm pores) was used to encourage capsular interactions with the membrane, because we hypothesized that the membrane detects changes in pore occlusion. No change in diffusion of fluorescein isothiocyanate (FITC)–immunoglobulin G (IgG) was seen when the FibroSensing elements were incorporated when compared with TPU-only membranes (fig. S1B and Supplementary Methods).

Monitoring of Matrigel and myofibroblast proliferation on FSDSR device using electrical impedance spectroscopy

Baseline FSDSR impedance measurements were taken in 1× phosphate-buffered saline (PBS). Impedance remained constant from 0.1 to 1000 Hz and decreased at higher frequencies (fig. S2, A to C). Impedance appears to be purely resistive for $f \leq 100$ Hz (table S1). The capacitive behavior of the FSDSR at higher frequencies, reflected by an arc on the complex plot and a peak in phase angle (fig. S2A), is expected to be caused by the conductive membrane/pore interface—this reaction is expected and provides no information on the environment surrounding the device (*33*, *34*). Therefore, changes in impedance were measured by assessing marker 1 (logarithm of the mean Z' for $f \leq 100$ Hz; Supplementary Methods), which quantifies the electrical resistivity of the medium in contact with the FibroSensing membrane.

Various concentrations of an extracellular matrix–rich basement membrane hydrogel (Matrigel: 30, 40, 50, and 60% w/v) were allowed to solidify on FSDSRs. The complex impedance plots show circular patterns with increases in arc size at each concentration (Fig. 2A). The system was predominantly resistive (fig. S3A, i and ii, and table S2), and marker 1 significantly increased with increased Matrigel concentrations (Fig. 2B).

WPMY-1 myofibroblasts were seeded and proliferated on FSDSRs for 7 days. Cell presence (Fig. 2C), viability (fig. S3B, i), and functionality (fig. S3B, ii) were monitored to confirm collagen deposition. The percentage of pores occluded qualitatively increased over time (fig. S3B, iii). An increase in impedance occurred from days 1 to 5 and 7 and days 3 to 7 (fig. S3C, i and ii). The system was predominantly resistive at $f \leq 100$ Hz (fig. S3C and table S3), and the same patterns were observed on the complex impedance plots (Fig. 2D). Marker 1 increased significantly as a function of time (Fig. 2E and table S4), showing that marker 1 is able to detect impedance changes related to cell density and collagen abundance over time.

Because the fibrotic capsule is highly cellularized, two densities of WPMY-1 myofibroblasts were seeded within 40% Matrigel to determine whether cell number affected signal output. The system

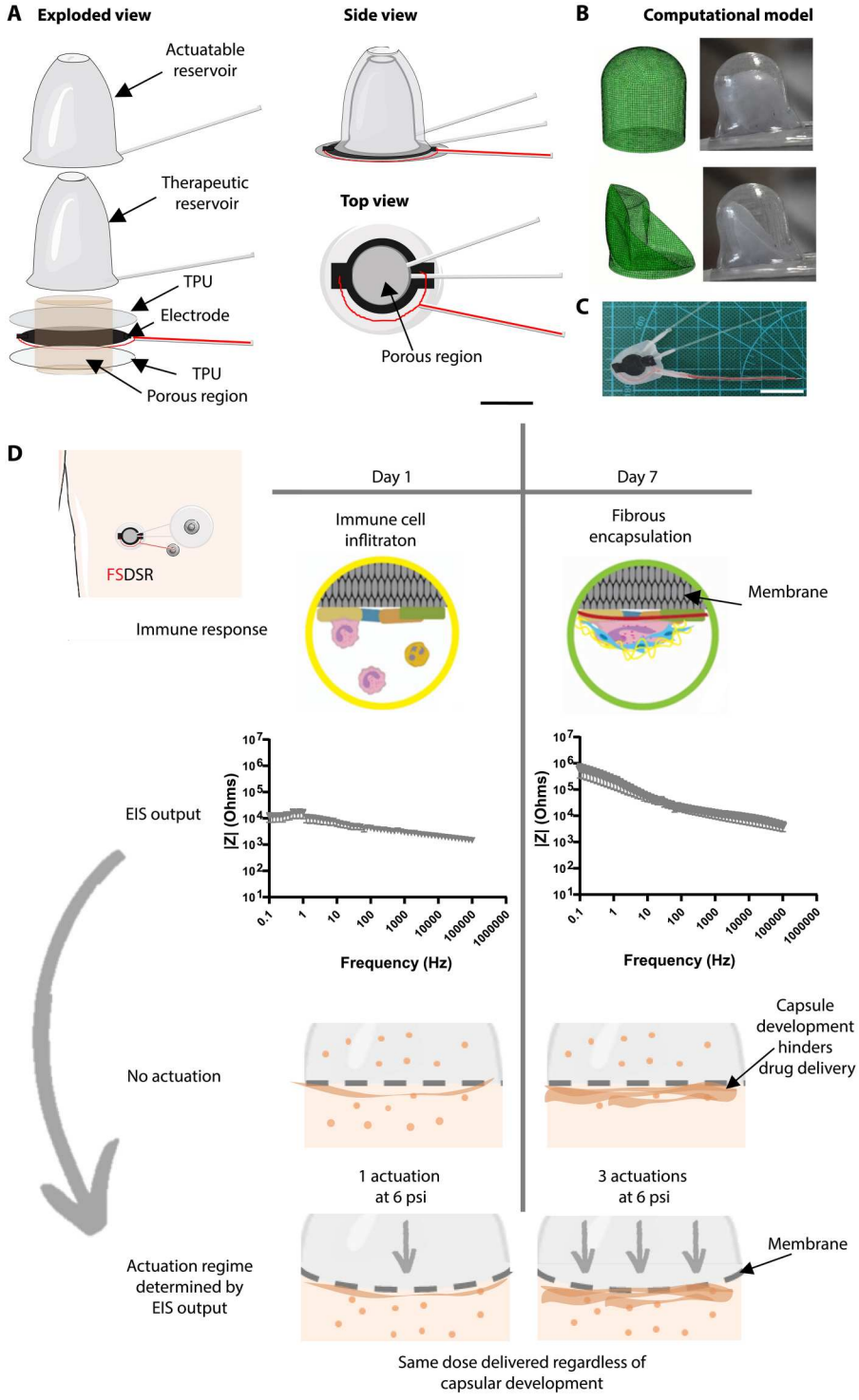

Fig. 1. An overview of the FSDSR device and mechanism of action. (**A**) Schematic of the FSDSR soft robotic drug delivery device (scale bar, 1 cm). (**B**) Computational model showing compression of inner therapeutic reservoir when the outer reservoir is pressurized, which can also be seen in vitro. (**C**) Image of the FSDSR device (scale bar, 2 cm). (**D**) Drug delivery devices fail because of occlusion as a result of the host foreign body response. The FSDSR senses changes in occlusion via electrical impedance spectroscopy. The FSDSR is capable of overcoming blockages by self-adapting its actuation regimen to sustain drug delivery over time, regardless of capsular development.

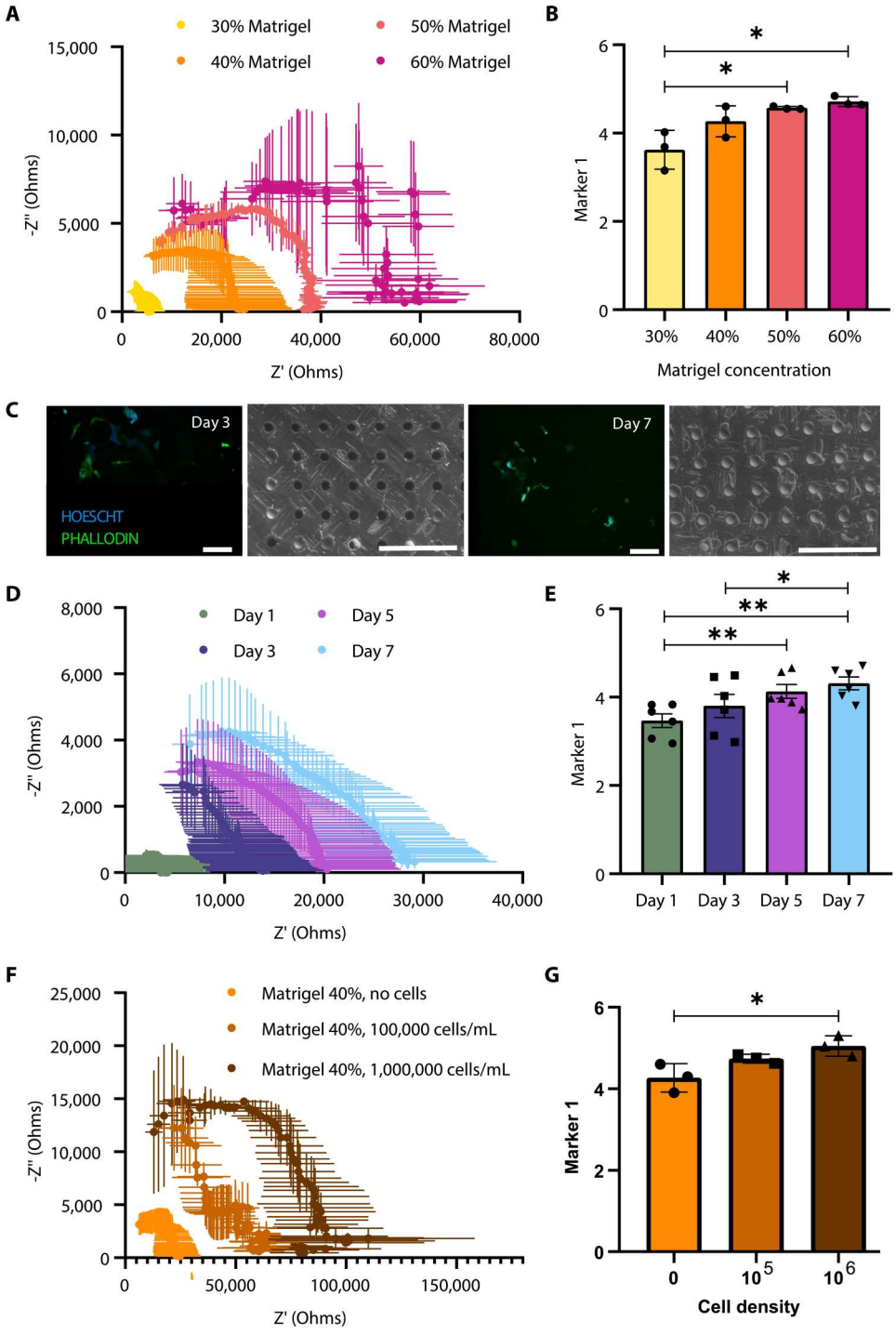

Fig. 2. FSDSR detects impedance changes in Matrigel, cellular presence, and density. (**A**) Complex impedance plot for Matrigel at each concentration (%). (**B**) Significant differences in marker 1 (logarithm of Z' for $f \leq 100$ Hz) observed between 30 and 50% (*P = 0.032) and 30 and 60% (*P = 0.021) (n = 3 per group). (**C**) WPMY-1 on device at days 3 and 7 (green, phalloidin; blue, Hoechst; scale bars, 100 μm). Scanning electron micrographs show the pore blockages (scale bars, 1 mm). (**D**) Complex impedance plot of WPMY-1 at days 1, 3, 5, and 7. (**E**) Marker 1 increases between days 1 and 5 (**P = 0.002), days 1 and 7 (**P = 0.004), and days 3 and 7 (*P = 0.015) (n = 6 per group). (**F**) Complex impedance plot of 40% Matrigel alone and seeded with 100,000 and 1,000,000 WPMY-1 cells/ml. (**G**) Marker 1 increases for 40% Matrigel alone to 40% Matrigel plus 1,000,000 cells/ml (*P = 0.020) (n = 3 per group). Mean ± SEM.

again behaved resistively at low frequencies (table S5). An increase in electrical impedance (Fig. 2F and fig. S3D, i and ii) and marker 1 (Fig. 2G) was seen between 40% Matrigel alone and Matrigel with a high density of cells (1,000,000 cells/ml). This highlighted the ability of the sensor to detect impedance changes relating to cellular presence and the extracellular matrix.

Monitoring fibrotic capsule development over time using the sensor-driven FSDSR device in a rodent model

FSDSRs were implanted in a rodent model for 7 days to investigate the ability of the sensor to monitor fibrotic capsule formation in real time (Fig. 3A). Changes occurred on the bode (Fig. 3B, i) and phase angle plots (Fig. 3B, ii). As phase peaked and |Z| decreased for $f \leq$ 100 Hz, the system could no longer be assumed to behave resistively; thus, marker 1 was not used to characterize this complex behavior (fig. S4A). This behavior was also reflected by an additional arc in the complex impedance plot observed in 21 of 40 measurements (fig. S4B), which was not present in vitro.

The capsular region (Fig. 3C) directly beneath the dome of the device and overlying membrane was reconstructed using segmentation (Mimics, Materialise, Leuven) from micro-computed tomography (micro-CT) (*1*, *35*). A time-dependent increase in mean capsular thickness (Fig. 3D, i) and thickness dot plots (fig. S4C) occurred. Because thickness was not always well captured using micro-CT, volumetric reconstructions of the fibrotic capsule were examined and also significantly increased over time (Fig. 3D, ii).

To account for the new behavior seen on the complex impedance plot, an equivalent circuit model [resistor (R) in series with two combinations of a constant phase element (CPE) in parallel with R] was closely fitted to the measured impedance data (*25*, *33*) using a custom nonlinear least square algorithm (Fig. 3, E and F) (*34*). R_{inf} quantifies the base resistance of the system, the first R_1/CPE_1 combination represents the electrochemical reaction at the conductive membrane/pore interface, and the second R_p/CPE_2 combination mirrors the medium contained inside the pore (Supplementary Methods). Fitted R_p was plotted for each time point (Fig. 3G) for the devices explanted on day 7. R_p increased between days 1 versus 3, 5, and 7 and between days 3 versus 7 for those devices. R_p did not always increase significantly between other time points. Importantly, R_p significantly increased as a function of time for all devices (table S6), showing that all devices sensed fibrotic capsule formation. Despite reflecting the same changes over time as marker 1 (fig. S4A), R_p should solely represent the electrical resistance of the capsule while reducing the noise from other capacitive behaviors (*34*). Capsular volume (Fig. 3H) and thickness (fig. S4D) both correlate to capsular electrical resistance R_p. No statistical differences between days 5 and 7 were observed from electrochemical impedance spectroscopy or micro-CT analysis, so day 5 was omitted in subsequent analyses. Scanning electron microscopy confirmed capsular ingrowth via interactions with FSDSRs. An overview of the device (yellow) is shown in situ (Fig. 4A). High-resolution investigation revealed an initial influx of cells into the device at day 1 (through the 100-μm pores). At day 7, collagenous material was present in the FSDSR pores. This change over time qualitatively confirmed dynamic changes in the FSDSR's surrounding environment.

Collagen fiber alignment was examined using polarized light microscopy to determine whether changes in the electrical impedance could be attributed to increased capsular alignment (Fig. 4B). No change in fiber thickness was seen (green/yellow, thin; red/orange, thick) (fig. S4, E and F). The overall collagen alignment of the fibrotic capsule, as measured by coherency, increased from implantation to days 3 and 7 (Fig. 4C), with a more organized capsule evident when qualitatively comparing days 1 and 7. An increase in total cell number, as analyzed using hematoxylin and eosin (H&E) staining, was evident (Fig. 4, D and E). Myofibroblasts and macrophages were present in the capsule at these early time points, as expected (Fig. 4, F and G).

Using the FibroSensing membrane to monitor implant actuation

A fatigue test revealed that FSDSRs could withstand 20,000 actuation cycles from 0 to 10 psi, with no change in baseline electrical impedance (fig. S5A and Supplementary Methods). Before and after fatigue (fig. S5B, i and ii), the devices (n = 3 per group) were burst pressure–tested and could withstand a pressure of 32 psi (5× > expected operating pressure). Impedance measurements were taken while the FSDSR was pneumatically actuating at various pressures (6 and 10 psi) (fig. S5C). Changes in sensor output from baseline were seen when the chamber was pressurized during the cycle. The ability of the membrane to monitor its own deformation during actuation could be harnessed as a measure of implant function over time. Anelasticity of the FibroSensing membrane occurred (within 30 min). This confirmed that the integrity of the membrane was not compromised.

Controlling drug delivery via soft robotics

The FSDSR uses pneumatic soft robotic actuations to deliver therapies through the porous membrane into the surrounding environment (Fig. 5A and Supplementary Methods). The pressure profile is customizable (triangular or trapezoidal) (Fig. 5B), with greater control being exhibited using a trapezoidal profile. Our model describes the release of fluid through the fibrotic capsule (fig. S6, A and B), showing that drug release can be controlled by the number of pores, actuation number, and pressure (fig. S6C).

To confirm our ability to tune drug release from the FSDSR by adjusting the number and magnitude of actuations, two concentrations of agarose gels were used (*36*–*40*). The permeability of the fibrotic capsule in vivo decreased (by half) from day 7 to day 28. Correspondingly, we used 0.3 and 0.6% agarose gels (permeability ratio of 2:1) to represent each time point (Fig. 5C and table S7). Shadowgraphy was used to quantify the release of a drug analog (methylene blue) after triangular actuations of varying amplitude (Fig. 5D). In both gels, the area covered by the dye increased as the applied pressure and the number of actuations increased (Fig. 5, E and F, and table S8). This demonstrated the ability of the FSDSR to control drug release by adjusting the actuation regimen.

Driving device function based on sensor signal

We posit that sensor signal can drive adjustments to the actuation regimen to maintain constant drug release despite fibrotic capsule formation. The electrical impedance of 0.3 and 0.6% agarose was measured (fig. S7, A to D). On the basis of sensor signal, a k-nearest neighbor (KNN) classifier was able to infer the correct agarose concentration with 78.8% accuracy (fig. S7E and table S9). Sensor signal from an agarose gel of unknown concentration was collected by a blinded operator (Fig. 5G) and input to the

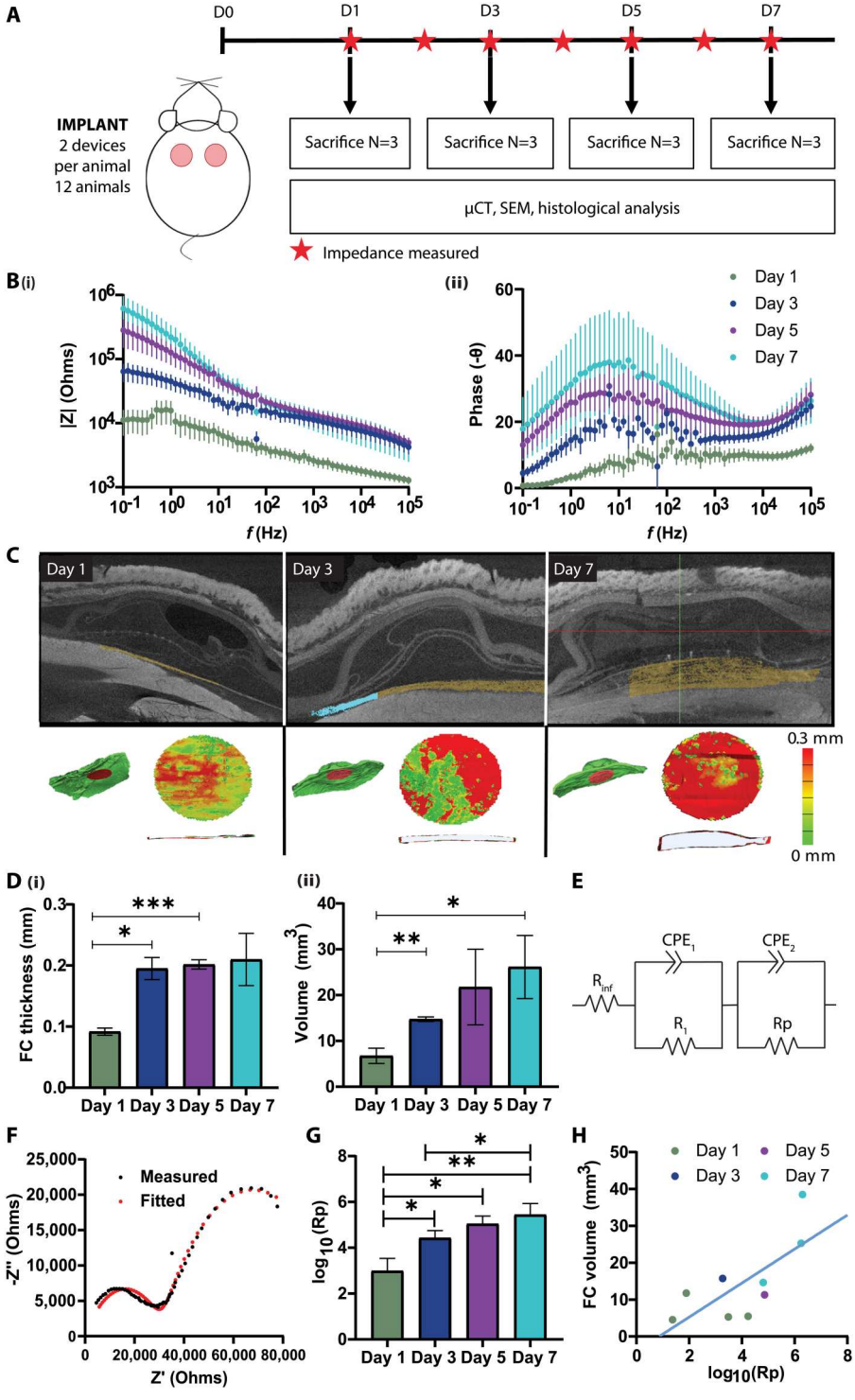

Fig. 3. FSDSR can detect changes in electrical impedance over time in a rodent model. (**A**) Two devices were subcutaneously implanted in 12 animals. At days 1, 3, 5, and 7, three animals were euthanized. (**B**) Bode (i) and phase angle plots (ii) in vivo. $n = 17$ at day 1; $n = 11$ at day 3; $n = 8$ at day 5; $n = 4$ at day 7. (**C**) Cross-sectional view of reconstructed capsule (yellow), with FSDSR (above) and surrounding soft tissue. 3D Mimics reconstruction of FSDSR (green) and extrapolated capsule (red) allows for surface shell elements from which thickness measurements are calculated. (**D**) (i) Average fibrotic capsule thickness increased between days 1 and 3 (*$P = 0.010$) and days 1 and 5 (***$P < 0.001$). (ii) Capsular volume ($n = 3$ per group) increased between days 1 and 3 (**$P = 0.007$) and day 1 and 7 (*$P = 0.050$). (**E**) Equivalent circuit model: R_{inf}, wire resistance; R_1//CPE_1, pore-membrane interface; R_p//CPE_2, pore resistance. (**F**) Measured data versus fitted model for one device at day 5. (**G**) Significant increase in logarithm of fitted R_p over time for devices explanted at day 7 [days 1 to 3 (*$P = 0.045$), days 1 to 5 (*$P = 0.025$), days 1 to 7 (**$P = 0.009$), and days 3 to 7 (*$P = 0.050$)]. Mean ± SEM. (**H**) Pearson's correlation (coefficient = 0.722) confirmed that fibrotic capsular volume correlates to pore electrical resistance R_p.

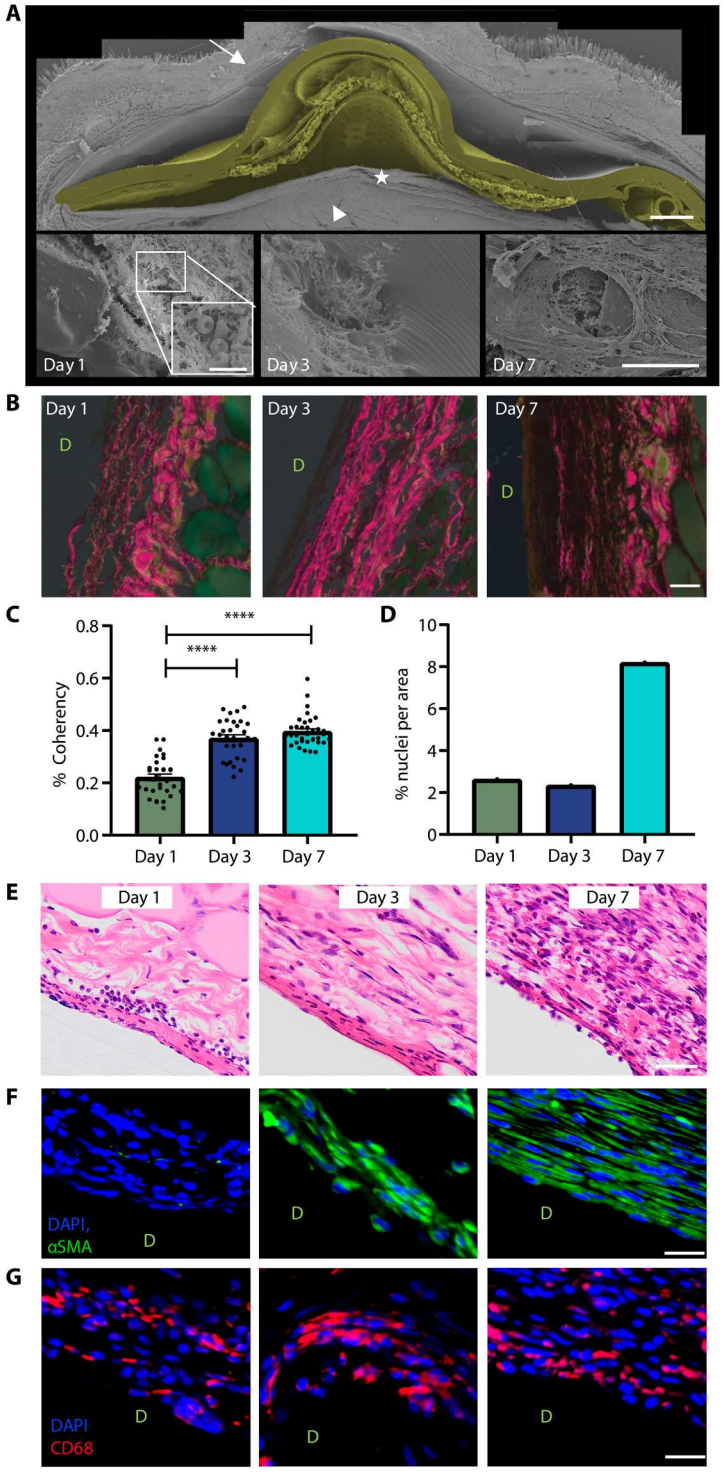

Fig. 4. Histological analysis of the fibrotic capsule development from days 1 to 7. (**A**) Scanning electron image of device in situ (yellow, device; arrow, skin; arrowhead, muscle; star, fibrotic capsule; scale bar, 1 mm). High magnification (scale bar, 10 μm) at day 1 shows the presence of red blood cells during early immune infiltration. Collagenous material, blocking a pore, is evident at day 7 (scale bar, 50 μm). (**B**) Polarized light micrographs of the fibrotic capsule (red/pink, capsule; green, muscle; D, device space; scale bar, 50 μm). (**C**) The overall capsule alignment, as measured by coherency (%), was increased from days 1 to 3 (****$P < 0.001$) and days 3 to 7 (****$P < 0.001$). (**D**) The % of nuclei per capsular area analyzed from (**E**) H&E staining qualitatively confirmed an increase in total cell number over time (D, device space; scale bar, 100 μm). (**F**) No WPMY-1 myofibroblasts were present at day 1. αSMA staining confirmed myofibroblast activation (day 3) and organization (day 7) (D, device space; blue, DAPI; green, αSMA; scale bar, 20 μm). (**G**) Macrophages (CD68) were present across all time points (D, device space; blue, DAPI; red, CD68; scale bar, 20 μm). Mean ± SEM.

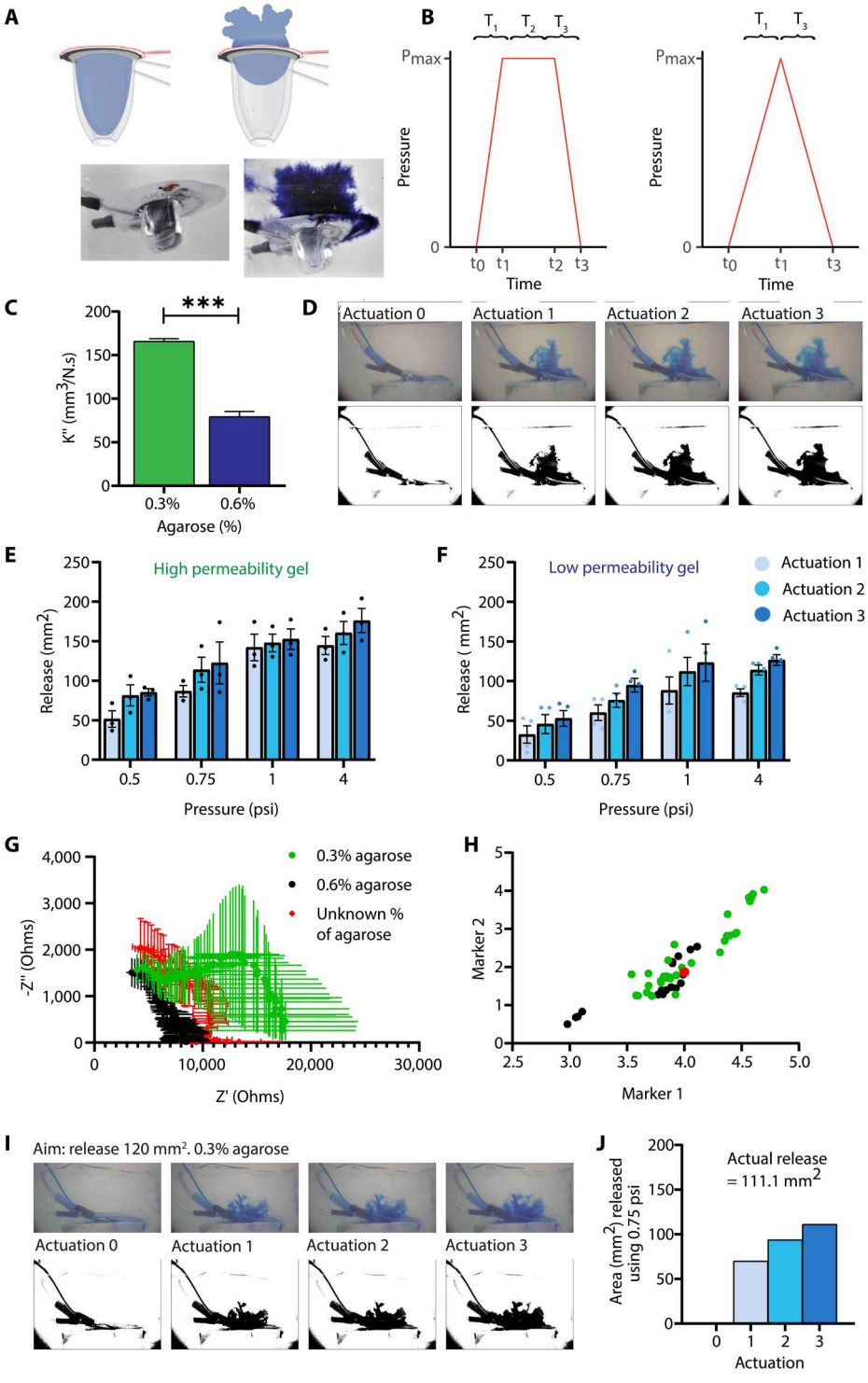

Fig. 5. FSDSR controls drug delivery via soft robotic actuations. (**A**) Schematic and photograph of drug release from the FSDSR. (**B**) Trapezoidal or triangular pressure profiles can induce drug release. (**C**) Hydraulic conductance of 0.6% was lower than 0.3% agarose (***$P = 0.0002$; $n = 3$ per group). (**D**) Raw (top) and processed (bottom) images of the release of methylene blue into 0.3% agarose at 1 psi. (**E** and **F**) Area increased as number of actuations and applied pressure increased in high (0.3%) and low (0.6%) agarose gels ($n = 3$ per group). (**G**) Complex impedance of 0.3 and 0.6% agarose. Blinded measurements taken with an unknown concentration (%) of agarose. (**H**) The *k*-nearest neighbor (KNN) classifer was successful in detecting the correct agarose concentration (0.3%) and recommending a desired actuation regimen to (**I**) release 120 mm^2 of methylene blue. (**J**) After three actuations at 0.75 psi, the actual amount of methylene blue released was 111.1 mm^2. Mean ± SEM.

KNN classifier. The KNN could predict the agarose concentration (57% accuracy shown in vitro) (Fig. 5H and table S10). On the basis of predicted agarose concentration, an optimal actuation regimen was predicted by the model to achieve a target methylene blue release (120 mm^2). The suggested regimen was three successive actuations (triangular pressure profile) at 0.75 psi, resulting in an actual release of 111.1 mm^2 (7.01% error) (Fig. 5, I and J). This demonstrates that electrochemical impedance spectroscopy can be used successfully to assess the FSDSR′s surrounding environment and inform a suggested actuation regimen to achieve a target release. With future development, including increased training data and model refinement, the FSDSR is envisaged to infer the thickness of the fibrotic capsule from its electrical resistance (fig. S8, A and B) and adjust its function accordingly.

Sustaining drug delivery despite fibrotic capsule formation

A COMSOL finite element model (diffusion and convection) was used to quantify drug release from the FSDSR when occluded by fibrotic capsules of various thicknesses (Fig. 6A). This capsule can be compensated for by applying successive actuations [Fig. 6B; goal = passive diffusion with no fibrotic capsule (green line); release with 75-μm fibrotic capsule (pink line); release using actuation (blue line)]. Actuations regimes at five thicknesses were simulated. At each thickness, pneumatic actuations were predicted to match or exceed the release goal (passive diffusion with no fibrotic capsule; Fig. 6C, green line). Otherwise, the release would decline as indicated by the orange line (Fig. 6C). A case-based reasoning algorithm allowed us to predict the most suitable regimen at each thickness (Fig. 6D). Where a significant reduction in passive drug release would have occurred, pneumatic actuations can maintain constant drug dosing. This demonstrates the potential of FSDSR for real-time adaptation of the actuation regimen for controlled drug delivery.

To determine the changes that occur in the capsule over time, for input into a computational model, capsule porosity measurements were analyzed from multiple species, sexes, and durations of implantation. It was found that capsule porosity did not vary substantially with species or sex (table S11; fig. S9, A to D; and Supplementary Methods), allowing capsule porosity at days 7, 28 (interpolated), and 58 to be inferred as 0.8, 0.54, and 0.3, respectively (Fig. 7, A to C, and table S12). Using COMSOL, custom actuation regimens could be deployed to mimic the release through an example of an early-stage fibrotic capsule at day 7 (Fig. 7A), as well as more developed fibrotic capsules at day 28 (Fig. 7B) and day 58 (Fig. 7C). Because the FSDSR harnesses the capabilities of soft robotics, which afford immense versatility with respect to the type and magnitude of output stimuli, the actuation regimen could be adjusted from a triangular to a rectangular pressure profile to reach the desired drug release (Fig. 7C). Actual capsule thickness and porosity at day 58 versus a "worst-case" scenario, taken to be the greatest fibrotic capsule thickness measured in vivo before capsule contracture (fig. S10), show the ability of the FSDSR to overcome either situation using soft robotics. Multiple porosities and thicknesses are one example that has been explored in this COMSOL model, but additional parameters in combination with in vivo studies of a longer duration would confirm the ability of the FSDSR to overcome any scenario. The final realization of the FSDSR is anticipated to operate as a closed-loop system, whereby the device measures the electrical resistance of the fibrotic capsule, infers the degree of occlusion of the porous membrane, and adjusts the actuation regimen to achieve the desired drug release profile (Fig. 7D).

DISCUSSION

We present FSDSR, an implantable soft robotic drug delivery device with inbuilt sensor capabilities. The abiotic/biotic interface can be continuously monitored in real time to inform subsequent pneumatically actuated drug delivery over the implant lifetime. By controlling actuation, the FSDSR allows modulation of drug dosing despite fibrotic capsule formation in vitro. We demonstrated the FSDSR′s ability to monitor changes in vivo, from initial cellular influx to capsular remodeling. Here, we have shown that an implantable sensor that uses electrochemical impedance spectroscopy has been incorporated in the membranous portion of a soft robotic drug delivery device.

Initially, we showed using Matrigel that the FSDSR is capable of conducting an electrical current and measuring changes within its external environment. Thereafter, we demonstrated that the collagen deposited by WPMY-1 myofibroblasts within the pores of the membrane could be detected. Although soluble collagen production remained constant over the course of the cellular study, an increase in extracellular material was seen to be blocking the pores. This increase in material accounts for the change in electrical impedance, because current flows in the form of ions in extracellular material (*25*, *33*), exhibiting conductive and capacitive behaviors (*25*). On complex impedance planes, both biological tissues and electrode/electrolyte interfaces are expected to cause arcs as a result of their capacitive behaviors (*33*). The electrical properties of a biological tissue can provide information about the cell population (*25*, *41*), because cell membranes can act as dielectric materials (*42*), and bound charges can lead to complex electrical behaviors (*25*). Cells are expected to impede current flow at low frequencies while being less resistive at higher frequencies (*25*, *33*). In all studies carried out in vitro, impedance was considered predominantly resistive at low frequencies. The capacitive behavior observed at $f > 100$ Hz is due to both the electrode/electrolyte interface and cell presence. The FSDSR device proved successful in detecting changes in its environment, in terms of both extracellular material and cell presence. By understanding this interaction at the abiotic/biotic interface within the pores of the FibroSensing membrane, we can monitor cellular and extracellular changes in electrical impedance that occur over time.

When implanted in vivo, the system did not behave purely resistively because we observed a second hemisphere on the complex impedance plots and a second peak in phase angle at low frequencies. This increase in capacitance at low frequencies was reflective of an increase in cell number/type in the surrounding environment (*25*, *33*, *43*) [macrophages in early days of fibrosis (*6*, *8*, *44*)]. Data fitting allowed us to extract information from the complex signals, because R_p (resistance of medium within the pores) increased over time to reflect capsular growth (*25*, *45*, *46*). The use of a mixed model, accounting for device and animal variability, confirmed an increase in impedance over time in all cases. This demonstrates that all devices sensed fibrotic capsule formation.

Correlating electrical impedance and biological changes is imperative to making the signal generated meaningful and actionable. Fibrotic capsule analysis revealed a time-dependent increase in capsular thickness. The initial stages of the foreign body response

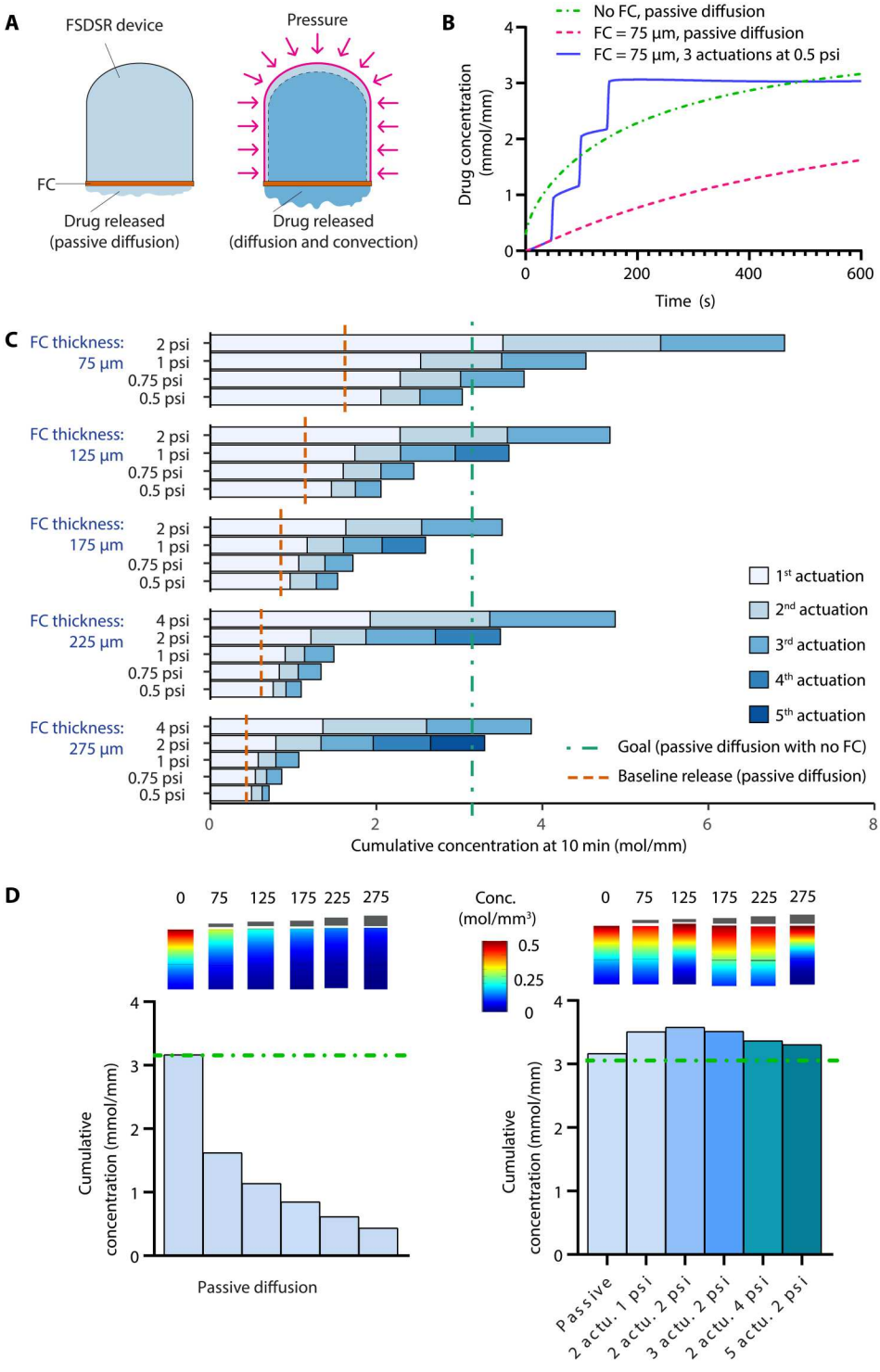

Fig. 6. FSDSR overcomes the foreign body response and sustains drug delivery. (**A**) Schematic of FSDSR modeled in COMSOL. (**B**) Drug release is lower when a fibrotic capsule (FC; 75 μm thick; pink line) hinders passive diffusion (compared with no capsule; green line). Pneumatic actuations compensate for this loss to reach the target drug release (blue line). (**C**) Database generated by COMSOL. Pneumatic actuations can match or exceed the release obtained with passive diffusion with no capsule (green line), at each capsule thickness. Green line, goal, no capsule, passive diffusion; red, release, passive diffusion with capsule of that specific thickness. (**D**) When delivered via passive diffusion, drug release is impeded as the fibrotic capsule grows. Case-based reasoning can find a suitable actuation regimen to maintain constant drug dosing despite fibrotic capsule growth.

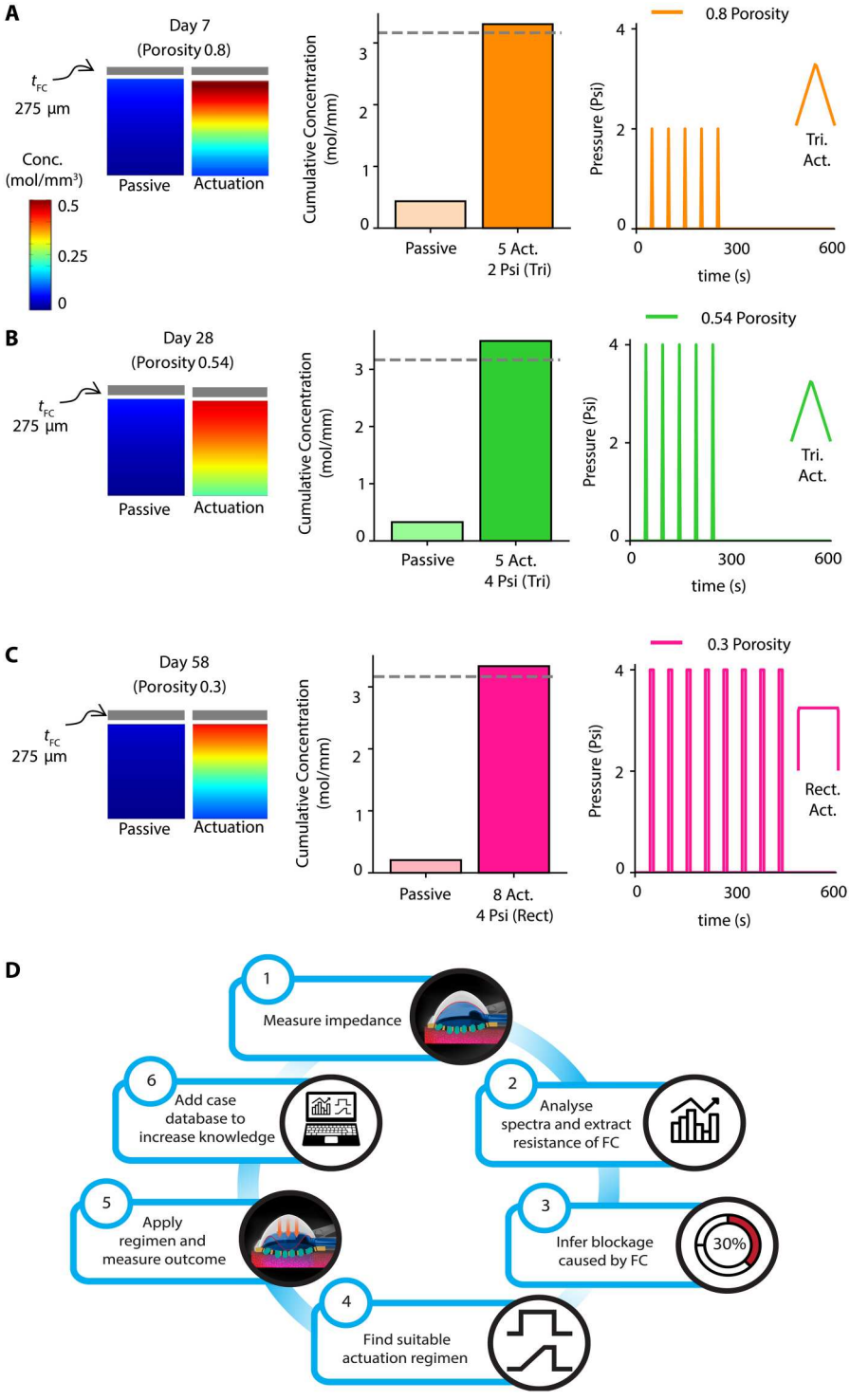

Fig. 7. FSDSR overcomes different stages of foreign body response using soft robotics. COMSOL model stimulated the variation in the fibrotic capsule (porosity, permeability, and diffusivity) after (**A**) 7 days, (**B**) 28 days, and (**C**) 58 days of implantation in vivo. By changing the number of actuations (Act.) and pneumatic profile (Tri. = triangular; Rect. = rectangular) applied to the FSDSR, an appropriate actuation regimen can be created to overcome the foreign body response to reach and/or exceed the desired drug outcome. (**D**) It is envisaged that the FSDSR will operate as part of a closed loop system where the capsule sensed in vivo will determine a suitable actuation regimen to deliver the desired drug dosage.

involve the influx of immune cells, deposition of collagenous material, and capsular remodeling (*44*). Both capsular thickness and volume correlated with the fitted R_p, displaying the ability of the FSDSR to monitor the progression of the foreign body response in real time.

Histological analysis provided insights into the biological processes that occurred in the developing fibrotic capsule. Myofibroblasts are contractile cells that are heavily involved in extracellular matrix reorganization in the fibrotic capsule (*47*, *48*). At day 1, myofibroblasts are not present in the fibrotic capsule surrounding the device, because fibroblasts are only being recruited to the site of inflammation (*49*, *50*). A relatively disorganized capsule can be seen at day 3, whereas the contractile capabilities of the myofibroblasts are beginning to occur at day 7 as the cells are visually elongated (*48*). This normal biological process (*44*) supports the hypothesis that the FSDSR does not cause excessive fibrosis; however, in future studies, the long-term biocompatibility of the FSDSR should be examined in larger animal models. These qualitative results corroborate the polarized light microscopy findings, which show the initial fibrotic capsule disorganization at day 1 and the more structured matrix at day 7. The ability of the FSDSR to detect these changes in its extracellular environment could be related to the collagen content and/or level of organization, which is constantly being remodeled. Like our Matrigel plus WPMY-1 myofibroblasts in vitro study, we also found an increase in total cell number over time in vivo, which partly accounts for our increased electrical impedance over time.

An increase in electrical impedance is seen depending on the level of deflection occurring in the FibroSensing membrane, which may be used as a measure of implant function. The ability of the FSDSR to monitor its own deformation provides another approach to improve current soft robotic drug delivery devices. In the case of fibrotic capsule formation and/or failure of the actuating component, a reduction in membrane deflection would be expected. Our FibroSensing membrane has the ability to detect such changes, providing unprecedented feedback on device function and performance.

The potential of the FSDSR to be used in a closed-loop system for sustained drug delivery was assessed in silico and in vitro. The effects of changing the pressure profile (trapezoidal or triangular) and number of actuations were the primary factors investigated here; however, future work could explore the effects of tuning the other actuation parameters (ramp up, plateau, ramp down, etc.). To mimic the porosity change seen between days 7 and 28, agarose was used to simulate a loss in device function. Agarose gels have been widely used to characterize drug release, in both passive and convection-enhanced delivery (*51*–*54*). We confirmed that soft robotic actuations can control drug release in agarose gels by increasing the pressure and/or the number of actuations, which resulted in increased methylene blue ejection. Although we had previously shown that intermittent actuation can enhance drug transport (*18*), here, we confirm that drug release can be finely controlled through the actuation regimen. The ability of the sensor to drive device function was investigated by classifying gel concentration on the basis of sensor signal via machine learning (*55*, *56*). The electrical impedance of agarose gels allowed the concentration to be inferred by a KNN classifier with 78.8% accuracy. This allowed us to finely control the release of methylene blue into an unknown concentration of agarose. The amount of methylene blue released was comparable to the release database, thus "closing the loop" in vitro (Fig. 5J).

For sensor signal to drive changes in the actuation regimen in a clinical setting, a robust control algorithm must evaluate the situation and find the most adequate solution. Here, case-based reasoning was used in silico to find the most suitable pressure and number of actuations to maintain constant drug dosing despite fibrotic capsule formation. We showed that the FSDSR can match or exceed the dose delivered via passive diffusion when no fibrotic capsule is present. If the actuation regimen was not modified, device function would decline with capsular growth. However, by using soft robotic actuations, the device can release more than the goal, regardless of the fibrotic capsule thickness (Fig. 6D). Here, case-based reasoning is used as a proof of concept. The limitations of using case-based reasoning are well characterized (*57*, *58*). Some of these include lower sensitivity, potential bias, and the inability to detect events outside the database, which in a human population would be required given the variability. To develop a clinically feasible closed-loop system in the setting of diabetes, a neural network (*59*) or complex series of algorithms is required that can adjust insulin delivery based on sensor readings [such as a proportional-integral-derivative (PID) control algorithm (*60*)]; filter the sensor signal [fault detection algorithm (*61*)]; integrate additional physiological signals, such as heart rate, to avoid scenarios such as exercise-related hypoglycemia (*60*); and handle patient inputs, such as mealtimes (*60*).

Previous studies have noted that the fibrotic capsule continues to mature and develop for months after implantation, with the permeability decreasing as the capsule becomes denser, further inhibiting drug release (*18*). To determine an actuation regimen that can overcome a more developed fibrotic capsule, capsular porosity was determined using histological analysis of samples from previous work (*18*, *35*) at days 28 and 58 (similarities in fibrotic capsules validated across rodent species and sex; table S11 and fig. S9). This showed that the FSDSR was capable of overcoming the fibrotic capsule in silico as late as day 58 (Fig. 7C).

The primary objective of this study was to assess whether the FSDSR could monitor the foreign body response in vivo by capturing information about the developing fibrotic capsule using electrochemical impedance spectroscopy to thereafter inform the actuation regimen. Although we successfully demonstrated the ability of the FSDSR to monitor foreign body response progression in vivo, as well as modulate drug delivery by changing its actuation regimen based on sensor signal in vitro, there are several limitations of the current work. Our in vivo findings from device implantation in the dorsal, posterior subcutaneous space of rats may not directly mimic the foreign body response in humans at different anatomical locations. Additional work is needed to understand how the foreign body response might vary in higher-order species and across implant location (*62*) and how such variability may affect the electrical impedance. Although rodent models have been extensively used to study the foreign body response (*63*, *64*), rodents are known to have different tissue composition in the space surrounding the implant and different metabolites in the interstitial fluid at implant interfaces compared with humans, which could influence fibrotic capsule formation and development. Future work will progress to a large animal model that is more relevant to humans (*65*, *66*), will ensure that electrical impedance can still be correlated with capsule development in both males and females over a range of ages,

and will aim to show the ability of the FSDSR to monitor foreign body response progression and subsequently modulate drug delivery by changing its actuation regimen in vivo. Looking forward, elucidating the relationship between sensor signal, fibrotic capsule formation, and device occlusion in humans may ultimately result in the clinical translation of this drug delivery device.

Overall, from this correlative study, we saw an increase in electrical impedance over time that is related to fibrotic capsule development. We observed an increase in capsular thickness and volume, a more organized fibrotic capsule, and an increase in total cell number from days 1 to 7. Further characterization at later time points in large animal models will yield additional data, which will inform the actuation regimen. This can ensure that regardless of capsular development, a suitable actuation-mediated drug delivery regimen can be used to overcome the limitations associated with the fibrotic capsule diffusion barrier. The utility of this system could be expanded to prevent device failure while ensuring sustained drug delivery over time in a wide range of medical device applications, some of which include implantable systems for infusion pumps and repeated targeted drug delivery to localized areas, which would be useful in certain types of peritoneal cancers (*67*). Another example involves the incorporation of additional sensors into the device, such as a continuous glucose monitor, to input data for a closed-loop insulin delivery system for the treatment of diabetes. As an implantable device that can monitor and respond to the foreign body response autonomously and in real time, the FSDSR has the potential to leverage the mechanical properties and capabilities of soft robotics to modulate its local environment and overcome the foreign body response drug diffusion barrier, one of the largest hurdles facing implantable medical technologies to date.

MATERIALS AND METHODS

FSDSR fabrication

A conductive layer of nonmetallic, highly conductive acrylic adhesive (ARcare 8881) was placed between two layers of 0.08-mm-thick TPU (HTM-8001-M and HTM-1001 polyether TPU film, American Polyfilm Inc.). Two pieces of wiring (RS PRO Red, 0.05 mm^2 Hook Up Wire; 15 cm) were inserted into catheter tubing (MRE080 Micro-Renathane, Braintree Scientific; 12 cm) and connected to the FibroSensing membrane. A 0.08- and 0.3-mm-thick TPU dome was thermoformed using a dental vacuum former. The 0.08-mm dome was placed inside the 0.3-mm dome to form two reservoirs. TPU catheter tubing (MRE037 Micro-Renathane, Braintree Scientific; 12 cm) was bonded to both reservoirs. The membrane and the reservoirs were heat-sealed at 166°C for 4 s (QXAi, Heat Transfer Machine, PowerPress). Laser-cut pores (100 μm) with 0.37-mm grid spacing (National Center for Laser Applications, University of Galway) were perforated through the circular section of the membrane using a Trumpf Trumicro 5050 Picosecond laser at ultraviolet 343-nm wavelength.

In vitro studies: Matrigel

Matrigel was thawed overnight at 4°C and kept on ice. Matrigel concentrations [30, 40, 50, and 60% (n = 3 per group)] were made using chilled high-glucose Dulbecco's modified Eagle's medium (DMEM) D5671 (Sigma-Aldrich). Matrigel solution (100 μl) was placed onto FSDSRs and immediately incubated (37°C; 2 min), then subsequently left at 20°C (20 min) to ensure homogeneity of the hydrogel. WPMY-1 myofibroblasts were cultured in the same supplemented DMEM. Cells (100,000 or 1,000,000 cells/ml) were diluted in 40% Matrigel and left to solidify at room temperature on the FSDSR devices.

In vitro studies: Cell proliferation and detection on FSDSRs

WPMY-1 human myofibroblast cell line (American Type Culture Collection, CRL-2845) was cultured in high-glucose DMEM (Sigma-Aldrich) supplemented with 5% fetal bovine serum (FBS), 1% penicillin-streptomycin, and 0.05% L-glutamine. The membrane was soaked in FBS (2 hours), washed with 1× PBS, and seeded with myofibroblasts (125,000 cells/ml; 24 hours at 37°C, 5% CO_2) on ethylene oxide–sterilized devices. Thereafter, collagen production was assessed using Sircol soluble collagen assay following the manufacturers' protocols at days 3, 5, and 7. Metabolic activity was assessed using an alamarBlue assay, as previously described (*57*). Cell presence was analyzed using scanning electron and confocal microscopy. For scanning electron microscopy, devices were washed in warmed 1× PBS and placed into primary fixative (2 hours). Sodium cacodylate (0.2 M) was applied (2 hours), and samples were dehydrated (30, 50, 70, 90, and 100% ethanol; 2 × 15 min). Images were taken using a Hitachi S-2600N scanning electron microscope with backscatter electron mode (vacuum 20 kV, electron beam 80, variable pressure 270 kPa). For confocal imaging, devices were washed in warmed 1× PBS and placed into 4% paraformaldehyde (10 min). PBS (1×) (3 × 5 min) and a 0.15% Triton X-100 solution were added (2 min). Bovine serum albumin (1%) was applied (30 min) and then washed in 1× PBS (3 × 5 min). Alexa Fluor 488 nm phalloidin (1:200; 60 min) was added, and devices were counterstained with Hoechst (1:1000; 10 min). Devices were mounted in a glass-bottom dish using fluoromount (F4680, Sigma-Aldrich) and observed using a spinning disc inverted confocal microscope (CSU22, Yokagawa) combined with Andor iQ 2.3 software.

In vivo preclinical study

Animal procedures were reviewed and approved according to ethical regulations by the Institutional Animal Care and Use Committee at Massachusetts Institute of Technology (MIT) (CAC protocol no. 0112-003-24). Twelve female Sprague Dawley rats (250 to 300 g, The Jackson Laboratory) were single-housed. Rats were anesthetized using isoflurane (1 to 3% in oxygen), and a single dose of sustained-release buprenorphine (1 mg/kg) was administered. Hair was removed from the back of the animal, and the surgical site was washed (3× betadine and 70% ethanol). One anterior (base of neck) and two posterior (1 cm lateral from spine) incisions were made for implantation of the ports and devices, respectively (fig. S1, C and D). After blunt dissection, two sterilized (ethylene oxide) FSDSR devices were subcutaneously implanted and sutured (7-0 prolene, nonabsorbable) to the underlying fascia. The skin was closed using interrupted sutures (Nylon, nonabsorbable), and the animal was allowed to recover on a heated pad. Electrical impedance was measured on days 0 to 7 while animals were anesthetized (isoflurane; 1 to 3% in oxygen). Three animals were sacrificed at days 1, 3, 5, and 7 (n = 3 per day). The device and surrounding tissue was explanted en bloc and fixed in 10% formalin at 4°C overnight and stored in 1× PBS.

Micro-CT, scanning electron microscopy, and histological analysis

One fixed sample per animal was transferred into 2.5% phosphomolybdic acid (Hopkin & Williams, 673400) to enable visualization of collagen-dense tissues (*68*). Skin was scored to facilitate passive uptake (7 days). Samples were scanned with Scanco Medical micro-CT 100 at high resolution. Dicom files were analyzed using Mimics research 18.0.525 software (Materialise). The capsular region of interest (area under the dome) was thresholded, and the background was removed using a Boolean operation. The resulting cyan mask was edited in a secondary view. A 7.4-to-7.6-mm circle was dropped in the center of the masked fibrotic capsule and calculated in 3D. An .STL file of this 3D reconstruction was imported into 3-Matic software (Materialise) and analyzed for capsular thickness. A fix wizard, smoothing factor (0.8), autoremesh, wall thickness analysis, and segmentation were performed, as previously described (*1*).

Samples were further dehydrated (90, 95, and 100% ethanol). Thereafter, they were bisected longitudinally and critically point-dried (EMITECH K850), mounted onto carbon tab aluminum stubs, and gold sputter–coated (Emscope SC500). Imaging was performed using a Hitachi S-2600N scanning electron microscope using a secondary electron detector (vacuum 15 kV, electron beam 50). Mountains Map 8 software was used to stitch and pseudo-color images.

One device per animal was selected at random and bisected longitudinally for histological analysis. Tissues were oriented, embedded (Leica wax embedder), and sectioned (7 μm thick) onto positively charged slides, deparaffinized in xylene, and brought to buffer through a series of graded alcohols. For immunofluorescence staining, slides were stained with an OPAL multiplex 7-color IHC staining (Akoya Biosciences) kit following the manufacturer's instructions. Primary antibodies were used in the following dilutions: CD68, 1:200 (Bio-Rad, MCA341R); CD31, 1:100 (Abcam, ab28364); αSMA, 1:500 (ab7817, Abcam); and spectral 4′,6-diamidino-2-phenylindole (DAPI). Slides were mounted (fluoromount; stored at 4°C). Slides were observed using a spinning disc inverted confocal microscope (CSU22, Yokagawa) combined with Andor iQ 2.3 software. For Picrosirius red staining, after rehydration, the samples were stained in 0.1% fast green (pH 7, Fast Green FCF; Sigma-Aldrich) (30 min) followed by 0.1% Sirius red in picric acid (Picrosirius red stain) (60 min) (*69*). Samples were dehydrated, cleared in xylene, and mounted (DPX). Using an Olympus BX4 polarized light microscope (Mason Technology Ltd., Dublin, Ireland), images were captured at 20×. The polarizing lenses were positioned on the light path before the sample and the second polarizer (analyzer) after the sample. Images were taken at 0° and 90° to maximum polarization. The two captured images were merged in ImageJ (Fiji, version 2.0.0). Mature and immature collagen was calculated through color thresholding by excluding the dark background (*70*). Dominant direction was determined using the Orientation J plugin on ImageJ (*71*). For H&E staining, after rehydration, samples were placed into hematoxylin (6 min), washed in water (2 min), and placed in eosin (6 min). Thereafter, the samples were rehydrated through graded alcohols, cleared in xylene, and mounted (DPX).

Modeling the deformation of the FSDSR

The reservoir was modeled using finite element software Abaqus/Explicit 2018 (Dassault Systèmes, RI, USA), with 8080 shell elements (three- and four-noded elements). A third-order Ogden hyperelastic material was used to model the TPU (*1*). The bottom edge of the membrane was fixed, and the rest of the reservoir surface was subjected to a linearly increased pressure up to 1 psi with a rate of 2 psi/s, and frictionless hard contact was applied throughout the whole model.

Impedance analysis

Impedance was analyzed and plotted using R (version 4.1.0) (*72*). Data points for which $-Z'' < 0$ were deleted (*73*), and phase angle θ was calculated as in Eq. 1

$$\theta = \left(\frac{180}{\pi}\right) a\tan\left(\frac{-Z''}{Z'}\right) \quad (1)$$

Resistivity was assumed if mean Z' was an order of magnitude higher than mean reactance $-Z''$, and if mean $\theta \asymp 0$, for $f \leq 100$ Hz. If considered resistive, the logarithm of mean Z', for $f \leq 100$ Hz, was used to reflect the changes in impedance in the system (marker 1). A linear mixed model (lmer) was used to capture changes in marker 1 over time while accounting for differences between devices (*74*).

To analyze the impedance in vivo (because the system did not behave resistively), an ideal circuit was fitted using a custom nonlinear least square algorithm (resistor in series with two combinations of a constant phase angle capacitor in parallel with a resistor). The following equation was fitted to the impedance data (Eq. 2).

$$R_{\text{inf}} + \frac{R_1}{R_1\text{CPE}_1(\omega j)^{n_1} + 1} + \frac{R_2}{R_2\text{CPE}_2(\omega j)^{n_1} + 1} \quad (2)$$

where ω is the angular frequency. The starting parameter values were approximated from the graphs and tightly bounded to ensure convergence (Supplementary Methods).

In vitro release studies

Agarose powder (Thermo Fisher Scientific, 9012-36-6) was prepared (deionized water; 100°C), cooled overnight, and broken using a spatula. Devices were submerged into 0.3 or 0.6% agarose, and impedance was measured. All technical replicates were used to test a KNN classifier (70% to train the model, 30% to validate; each set was selected randomly 100 times to calculate the mean accuracy). The KNN classifier was constructed using the ctree() function by partykit (*75*) and correlated agarose concentration, as a factor, to markers 1 and 2. Accuracy was calculated by counting the number of correct predictions during validation.

To measure the hydraulic conductance of the two gels, FSDSR devices were filled with methylene blue and placed into agarose gel. A constant pressure of 1 psi was applied to the actuatable reservoir (ElveFlow, OB1 MK3+). Discharged volume of methylene blue was plotted versus time. Linear trend lines were fitted, and their slopes, equivalent to the discharge flow rate (Q), served to calculate the hydraulic conductance K of the system (Eq. 3):

$$K'' = \frac{Q}{A_m P} \quad (3)$$

where A_m is the area of the membrane (78.54 mm^2) and P is the pressure applied (*76*).

Methylene blue–filled FSDSRs were placed into agarose gels. Triangular actuation profiles (5-s ramp up and down; 45-s break) were applied. Images before and after each actuation were acquired and converted into black and white (DinoLite Premier Camera 20-250×, DinoCapture 2.0 version 1.5.42). Release profiles were plotted by subtracting the initial number of black pixels from the number of counted pixels (converted to mean mm^2).

Case-based closed-loop system in vitro

A blinded operator measured the impedance of an unknown agarose gel and input the collected impedance data into the KNN classifier. The KNN classifier predicted the gel concentration (using markers 1 and 2). The database was constructed using released methylene blue into 0.3 and 0.6% agarose (Fig. 5E). An algorithm (case-based reasoning) recommended a regimen that was subsequently applied by the operator to release methylene blue into the same gel. Once actuated, images were collected and treated to quantify the release of the dye and compare its value with an arbitrary goal (120 mm^2).

Case-based closed-loop system in silico

A case-based reasoning system was evaluated by constructing a database consisting of a long-format data frame where each line contained information on fibrotic capsule thickness, actuation pressure, number of actuations, and predicted drug release output. An algorithm was produced to find the most adequate actuation regimen at each fibrotic capsule thickness to obtain a release as close as possible, but always superior, to the release obtained with passive diffusion with no capsule (diffusion on day 0 before fibrotic capsule formation).

In silico release studies

Drug transport and release from the FSDSR under different actuation regimes was simulated using COMSOL Multiphysics (Cambridge, UK). The 2D model consisted of the dome-shaped FSDSR, porous fibrotic capsule, and an outer rectangular fluid domain representing the FSDSR's surrounding target site (Fig. 6A). The thickness of the porous capsule varied from 75 to 275 μm (in vivo range). An arbitrary drug concentration of 1 mol/mm^3 was prescribed to the FSDSR, whereas the other domains were set to zero to monitor the release from the reservoir.

The fluid flow through the porous medium was defined using the Brinkman equation. The FSDSR and outer fluid were modeled as fluid domains of density 997 kg/m^3 and viscosity 8.9 $\times 10^{-4}$ Pa·s. The diffusivity, porosity, and permeability were varied to capture different stages in foreign body response (table S12). The porosity at day 28 was interpolated given the linear decrease in porosity between days 7 and 58. In addition, at day 28, the permeability was interpolated assuming a linear relationship between the resistance to flow at day 7 and more developed stages of scar tissue formation (*18*, *77*). The FSDSR was actuated in silico by uniformly applying the pneumatic regimen to the surface of the reservoir, whereas a zero-pressure outlet was defined at the base of the outer fluid domain. The passive diffusion through the fibrotic capsule at different stages in vivo (varying thickness and porosity) was simulated to show the capsule's resistance to drug release without actuation. In addition, the passive diffusion from the FSDSR when there was no fibrotic capsule was considered to mimic the idealized diffusion on day 0 before fibrotic capsule formation. To capture the drug release through the resistive fibrotic capsule to the target site, the concentration over a 10-min period was extracted from a fixed region in the outer fluid domain.

Statistical analysis

Statistical tests were performed in R (version 4.1.0). Parametric and nonparametric tests were applied (based on Shapiro-Wilk normality). One- or two-sided Student's *t* tests with Welsch correction were used. For the linear mixed models, the summ() function by jtools was used (*78*). Statistical significance was accepted when $P < 0.05$. The statistical tool G*Power (3.1.9.7) was used to calculate statistical power (0.9987) (*79*, *80*).

Supplementary Materials

This PDF file includes:

Methods
Figs. S1 to S10
Tables S1 to S12

Other Supplementary Material for this manuscript includes the following:

Movies S1 to S5
MDAR Reproducibility Checklist

REFERENCES AND NOTES

1. E. B. Dolan, C. E. Varela, K. Mendez, W. Whyte, R. E. Levey, S. T. Robinson, S. E. Rothenbucher, E. Maye, Y. Fan, R. Wylie, M. Monaghan, P. Dockery, G. P. Duffy, E. Roche, An actuatable soft reservoir modulates host foreign body response. *Sci. Robot.* **4**, eaax7043 (2019).
2. S. Guo, L. A. DiPietro, Factors affecting wound healing. *J. Dent. Res.* **89**, 219–229 (2010).
3. M. R. Major, V. W. Wong, E. R. Nelson, M. T. Longaker, G. C. Gurtner, The foreign body response. *Plast. Reconstr. Surg.* **135**, 1489–1498 (2015).
4. S. Barrientos, O. Stojadinovic, M. S. Golinko, H. Brem, M. Tomic-Canic, PERSPECTIVE ARTICLE: Growth factors and cytokines in wound healing. *Wound Repair Regen.* **16**, 585–601 (2008).
5. Y. Onuki, U. Bhardwaj, F. Papadimitrakopoulos, D. J. Burgess, A review of the biocompatibility of implantable devices: Current challenges to overcome foreign body response. *J. Diabetes Sci. Technol.* **2**, 1003–1015 (2008).
6. Y. K. Kim, E. Y. Chen, W. F. Liu, Biomolecular strategies to modulate the macrophage response to implanted materials. *J. Mater. Chem. B* **4**, 1600–1609 (2016).
7. Z. Sheikh, P. J. Brooks, O. Barzilay, N. Fine, M. Glogauer, Macrophages, foreign body giant cells and their response to implantable biomaterials. *Materials* **8**, 5671–5701 (2015).
8. J. M. Morais, F. Papadimitrakopoulos, D. J. Burgess, Biomaterials/tissue interactions: Possible solutions to overcome foreign body response. *AAPS J.* **12**, 188–196 (2010).
9. R. Hernandez-Pando, Q. L. Bornstein, D. Aguilar Leon, E. H. Orozco, V. K. Madrigal, E. Martinez Cordero, Inflammatory cytokine production by immunological and foreign body multinucleated giant cells. *Immunology* **100**, 352–358 (2000).
10. M. N. Avula, D. W. Grainger, Addressing medical device challenges with drug–device combinations, in *Drug-Device Combinations for Chronic Diseases* (Wiley, 2015), pp. 1–38.
11. D. Zhang, Q. Chen, Y. Bi, H. Zhang, M. Chen, J. Wan, C. Shi, W. Zhang, J. Zhang, Z. Qiao, J. Li, S. Chen, R. Liu, Bio-inspired poly-DL-serine materials resist the foreign-body response. *Nat. Commun.* **12**, 5327 (2021).
12. A. J. Vegas, O. Veiseh, J. C. Doloff, M. Ma, H. H. Tam, K. Bratlie, J. Li, A. R. Bader, E. Langan, K. Olejnik, P. Fenton, J. W. Kang, J. Hollister-Locke, M. A. Bochenek, A. Chiu, S. Siebert, K. Tang, S. Jhunjhunwala, S. Aresta-Dasilva, N. Dholakia, R. Thakrar, T. Vietti, M. Chen, J. Cohen, K. Siniakowicz, M. Qi, J. McGarrigle, S. Lyle, D. M. Harlan, D. L. Greiner, J. Oberholzer, G. C. Weir, R. Langer, D. G. Anderson, Combinatorial hydrogel library enables identification of materials that mitigate the foreign body response in primates. *Nat. Biotechnol.* **34**, 345–352 (2016).
13. L. Zhang, Z. Cao, T. Bai, L. Carr, J. R. Ella-Menye, C. Irvin, B. D. Ratner, S. Jiang, Zwitterionic hydrogels implanted in mice resist the foreign-body reaction. *Nat. Biotechnol.* **31**, 553–556 (2013).

14. M. A. Bochenek, O. Veiseh, A. J. Vegas, J. J. McGarrigle, M. Qi, E. Marchese, M. Omami, J. C. Doloff, J. Mendoza-Elias, M. Nourmohammadzadeh, A. Khan, C.-C. Yeh, Y. Xing, D. Isa, S. Ghani, J. Li, C. Landry, A. R. Bader, K. Olejnik, M. Chen, J. Hollister-Lock, Y. Wang, D. L. Greiner, G. C. Weir, B. L. Strand, A. M. A. Rokstad, I. Lacik, R. Langer, D. G. Anderson, J. Oberholzer, Alginate encapsulation as long-term immune protection of allogeneic pancreatic islet cells transplanted into the omental bursa of macaques. *Nat. Biomed. Eng.* **2**, 810–821 (2018).
15. J. Saad, D. Mathew, *Nonsteroidal Anti-Inflammatory Drugs Toxicity* (StatPearls Publishing, 2018).
16. S. Farah, J. C. Doloff, P. Müller, A. Sadraei, H. J. Han, K. Olafson, K. Vyas, H. H. Tam, J. Hollister-Lock, P. S. Kowalski, M. Griffin, A. Meng, M. McAvoy, A. C. Graham, J. McGarrigle, J. Oberholzer, G. C. Weir, D. L. Greiner, R. Langer, D. G. Anderson, Long-term implant fibrosis prevention in rodents and non-human primates using crystallized drug formulations. *Nat. Mater.* **18**, 892–904 (2019).
17. C. A. Cezar, E. T. Roche, H. H. Vandenburgh, G. N. Duda, C. J. Walsh, D. J. Mooney, Biologic-free mechanically induced muscle regeneration. *Proc. Natl. Acad. Sci. U.S.A.* **113**, 1534–1539 (2016).
18. W. Whyte, D. Goswami, S. X. Wang, Y. Fan, N. A. Ward, R. E. Levey, R. Beatty, S. T. Robinson, D. Sheppard, R. O'Connor, D. S. Monahan, K. L. Mendez, C. E. Varela, M. A. Horvath, R. Wylie, J. O'Dwyer, D. A. Domingo-Lopez, A. S. Rothman, G. P. Duffy, E. B. Dolan, E. T. Roche, Dynamic actuation enhances transport and extends therapeutic lifespan in an implantable drug delivery platform. *Nat. Commun.* **13**, 4496 (2022).
19. B. R. Seo, C. J. Payne, S. L. McNamara, B. R. Freedman, B. J. Kwee, S. Nam, I. de Lázaro, M. Darnell, J. T. Alvarez, M. O. Dellacherie, H. H. Vandenburgh, C. J. Walsh, D. J. Mooney, Skeletal muscle regeneration with robotic actuation-mediated clearance of neutrophils. *Sci. Transl. Med.* **13**, eabe8868 (2021).
20. J. Lee, K. Henderson, M. W. Massidda, M. Armenta-Ochoa, B. G. Im, A. Veith, B.-K. Lee, M. Kim, P. Maceda, E. Yoon, L. Samarneh, M. Wong, A. K. Dunn, J. Kim, A. B. Baker, Mechanobiological conditioning of mesenchymal stem cells for enhanced vascular regeneration. *Nat. Biomed. Eng.* **5**, 89–102 (2021).
21. G. Yang, H.-J. Im, J. H.-C. Wang, Repetitive mechanical stretching modulates IL-1beta induced COX-2, MMP-1 expression, and PGE2 production in human patellar tendon fibroblasts. *Gene* **363**, 166–172 (2005).
22. K. Y. Lee, M. C. Peters, D. J. Mooney, Controlled drug delivery from polymers by mechanical signals. *Adv. Mater.* **13**, 837–839 (2001).
23. E. Barsoukov, J. R. Macdonald, *Impedance Spectroscopy: Theory, Experiment, and Applications* (John Wiley and Sons, 2005).
24. J. R. Macdonald, Impedance spectroscopy. *Ann. Biomed. Eng.* **20**, 289–305 (1992).
25. D. A. Dean, T. Ramanathan, D. Machado, R. Sundararajan, Electrical impedance spectroscopy study of biological tissues. *J. Electrostat.* **66**, 165–177 (2008).
26. E. Gersing, Impedance spectroscopy on living tissue for determination of the state of organs. *Bioelectrochem. Bioenerg.* **45**, 145–149 (1998).
27. F. B. Karp, N. A. Bernotski, T. I. Valdes, K. F. Böhringer, B. D. Ratner, Foreign body response investigated with an implanted biosensor by in situ electrical impedance spectroscopy. *IEEE Sens. J.* **8**, 104–112 (2008).
28. N. Lewis, C. Lahuec, S. Renaud, E. Mcadams, P. Bogonez-Franco, C. Lethias, S. Kellouche, F. Carreiras, A. Pinna, A. Histace, Relevance of impedance spectroscopy for the monitoring of implant-induced fibrosis: A preliminary study, in *2015 IEEE Biomedical Circuits and Systems Conference (BioCAS)* (IEEE, 2015).
29. T. Süselbeck, H. Thielecke, J. Köchlin, S. Cho, I. Weinschenk, J. Metz, M. Borggrefe, K. K. Haase, Intravascular electric impedance spectroscopy of atherosclerotic lesions using a new impedance catheter system. *Basic Res. Cardiol.* **100**, 446–452 (2005).
30. M. Lin, H. Hu, S. Zhou, S. Xu, Soft wearable devices for deep-tissue sensing. *Nat. Rev. Mater.* **7**, 850–869 (2022).
31. O. A. Araromi, M. A. Graule, K. L. Dorsey, S. Castellanos, J. R. Foster, W. H. Hsu, A. E. Passy, J. J. Vlassak, J. C. Weaver, C. J. Walsh, R. J. Wood, Ultra-sensitive and resilient compliant strain gauges for soft machines. *Nature* **587**, 219–224 (2020).
32. R. J. Soto, E. P. Merricks, D. A. Bellinger, T. C. Nichols, M. H. Schoenfisch, Influence of diabetes on the foreign body response to nitric oxide-releasing implants. *Biomaterials* **157**, 76–85 (2018).
33. E. T. McAdams, J. Jossinet, Tissue impedance: A historical overview. *Physiol. Meas.* **16**, A1–A13 (1995).
34. J. R. Macdonald, W. B. Johnson, in *Impedance Spectroscopy* (John Wiley & Sons Ltd., 2018), pp. 1–20.
35. R. Beatty, C.-E. Lu, J. Marzi, R. E. Levey, D. Carvajal Berrio, G. Lattanzi, R. Wylie, R. O'Connor, E. Wallace, G. Ghersi, M. Salamone, E. B. Dolan, S. L. Layland, K. Schenke-Layland, G. P. Duffy, The foreign body response to an implantable therapeutic reservoir in a diabetic rodent model. *Tissue Eng. Part C Methods* **27**, 515–528 (2021).
36. W. Y. Gu, H. Yao, C. Y. Huang, H. S. Cheung, New insight into deformation-dependent hydraulic permeability of gels and cartilage, and dynamic behavior of agarose gels in confined compression. *J. Biomech.* **36**, 593–598 (2003).
37. E. J. Szili, J. S. Oh, S. H. Hong, A. Hatta, R. D. Short, Probing the transport of plasma-generated RONS in an agarose target as surrogate for real tissue: Dependency on time, distance and material composition. *J. Phys. D Appl. Phys.* **48**, 202001 (2015).
38. R. Pomfret, G. Miranpuri, K. Sillay, The substitute brain and the potential of the gel model. *Ann. Neurosci.* **20**, 118–122 (2013).
39. G. Scionti, M. Moral, M. Toledano, R. Osorio, J. D. G. Durán, M. Alaminos, A. Campos, M. T. Lõpez-Lõpez, Effect of the hydration on the biomechanical properties in a fibrin-agarose tissue-like model. *J. Biomed. Mater. Res. A* **102**, 2573–2582 (2014).
40. J. N. Mehta, G. R. McRoberts, C. G. Rylander, Controlled catheter movement affects dye dispersal volume in agarose gel brain phantoms. *Pharmaceutics* **12**, 753 (2020).
41. S. Tonello, A. Bianchetti, S. Braga, C. Almici, M. Marini, G. Piovani, M. Guindani, K. Dey, L. Sartore, F. Re, D. Russo, E. Cantù, N. F. Lopomo, M. Serpelloni, E. Sardini, Impedance-based monitoring of mesenchymal stromal cell three-dimensional proliferation using aerosol jet printed sensors: A tissue engineering application. *Materials* **13**, 2231 (2020).
42. K. S. Cole, Electric phase angle of cell membranes. *J. Gen. Physiol.* **15**, 641–649 (1932).
43. H. P. Schwan, Electrical properties of tissue and cell suspensions. *Adv. Biol. Med. Phys.* **5**, 147–209 (1957).
44. J. M. Anderson, A. Rodriguez, D. T. Chang, Foreign body reaction to biomaterials. *Semin. Immunol.* **20**, 86–100 (2008).
45. R. Magisetty, S. M. Park, New era of electroceuticals: Clinically driven smart implantable electronic devices moving towards precision therapy. *Micromachines* **13**, 161 (2022).
46. L. Wang, K. Jiang, G. Shen, Wearable, implantable, and interventional medical devices based on smart electronic skins. *Adv. Mater. Technol.* **6**, 2100107 (2021).
47. K. Bharath Rao, N. Malathi, S. Narashiman, S. T. Rajan, Evaluation of myofibroblasts by expression of alpha smooth muscle actin: A marker in fibrosis, dysplasia and carcinoma. *J. Clin. Diagn. Res.* **8**, ZC14–ZC17 (2014).
48. N. Noskovicova, B. Hinz, P. Pakshir, Implant fibrosis and the underappreciated role of myofibroblasts in the foreign body reaction. *Cell* **10**, 1794 (2021).
49. P. Bainbridge, Wound healing and the role of fibroblasts. *J. Wound Care* **22**, 407–412 (2013).
50. A. V. Shinde, C. Humeres, N. G. Frangogiannis, The role of α-smooth muscle actin in fibroblast-mediated matrix contraction and remodeling. *Biochim. Biophys. Acta Mol. Basis Dis.* **1863**, 298–309 (2017).
51. K. Samprovalaki, P. T. Robbins, P. J. Fryer, Investigation of the diffusion of dyes in agar gels. *J. Food Eng.* **111**, 537–545 (2012).
52. E. M. Johnson, D. A. Berk, R. K. Jain, W. M. Deen, Hindered diffusion in agarose gels: Test of effective medium model. *Biophys. J.* **70**, 1017–1023 (1996).
53. A. A. Linninger, M. R. Somayaji, M. Mekarski, L. Zhang, Prediction of convection-enhanced drug delivery to the human brain. *J. Theor. Biol.* **250**, 125–138 (2008).
54. M. T. Krauze, R. Saito, C. Noble, M. Tamas, J. Bringas, J. W. Park, M. S. Berger, K. Bankiewicz, Reflux-free cannula for convection-enhanced high-speed delivery of therapeutic agents. *J. Neurosurg.* **103**, 923–929 (2005).
55. R. M. Hathout, *Machine Learning Methods in Drug Delivery* (Elsevier Inc., 2021).
56. M. Tiitta, V. Tiitta, J. Heikkinen, R. Lappalainen, L. Tomppo, Classification of wood chips using electrical impedance spectroscopy and machine learning. *Sensors* **20**, 1076 (2020).
57. P. Herrero, P. Pesl, M. Reddy, N. Oliver, P. Georgiou, C. Toumazou, Advanced insulin bolus advisor based on run-to-run control and case-based reasoning. *IEEE J. Biomed. Heal. Informatics* **19**, 1087–1096 (2015).
58. M. Reddy, P. Pesl, M. Xenou, C. Toumazou, D. Johnston, P. Georgiou, P. Herrero, N. Oliver, Clinical safety and feasibility of the advanced bolus calculator for type 1 diabetes based on case-based reasoning: A 6-week nonrandomized single-arm pilot study. *Diabetes Technol. Ther.* **18**, 487–493 (2016).
59. K. Y. Ngiam, I. W. Khor, Big data and machine learning algorithms for health-care delivery. *Lancet Oncol.* **20**, e262–e273 (2019).
60. C. K. Boughton, R. Hovorka, New closed-loop insulin systems. *Diabetologia* **64**, 1007–1015 (2021).
61. F. J. Doyle III, L. M. Huyett, J. B. Lee, H. C. Zisser, E. Dassau, Closed-loop artificial pancreas systems: Engineering the algorithms. *Diabetes Care* **37**, 1191–1197 (2014).
62. G. P. Duffy, S. T. Robinson, R. O'Connor, R. Wylie, C. Mauerhofer, G. Bellavia, S. Straino, F. Cianfarani, K. Mendez, R. Beatty, R. Levey, J. O'Sullivan, L. McDonough, H. Kelly, E. T. Roche, E. B. Dolan, Implantable therapeutic reservoir systems for diverse clinical applications in large animal models. *Adv. Healthc. Mater.* **9**, 2000305 (2020).
63. O. Veiseh, A. J. Vegas, Domesticating the foreign body response: Recent advances and applications. *Adv. Drug Deliv. Rev.* **144**, 148–161 (2019).
64. A. J. Vegas, O. Veiseh, M. Gürtler, J. R. Millman, F. W. Pagliuca, A. R. Bader, J. C. Doloff, J. Li, M. Chen, K. Olejnik, H. H. Tam, S. Jhunjhunwala, E. Langan, S. Aresta-Dasilva, S. Gandham,

J. J. McGarrigle, M. A. Bochenek, J. Hollister-Lock, J. Oberholzer, D. L. Greiner, G. C. Weir, D. A. Melton, R. Langer, D. G. Anderson, Long-term glycemic control using polymer-encapsulated human stem cell-derived beta cells in immune-competent mice. *Nat. Med.* **22**, 306–311 (2016).

65. N. Wisniewski, N. Rajamand, U. Adamsson, P. E. Lins, W. M. Reichert, B. Klitzman, U. Ungerstedt, Analyte flux through chronically implanted subcutaneous polyamide membranes differs in humans and rats. *Am. J. Physiol. Endocrinol. Metab.* **282**, E1316–E1323 (2002).
66. L. Chung, D. R. Maestas Jr., A. Lebid, A. Mageau, G. D. Rosson, X. Wu, M. T. Wolf, A. J. Tam, I. Vanderzee, X. Wang, J. I. Andorko, H. Zhang, R. Narain, K. Sadtler, H. Fan, D. Čiháková, C. J. Le Saux, F. Housseau, D. M. Pardoll, J. H. Elisseeff, Interleukin 17 and senescent cells regulate the foreign body response to synthetic material implants in mice and humans. *Sci. Transl. Med.* **12**, eaax3799 (2020).
67. C. Carlier, A. Mathys, E. De Jaeghere, M. Steuperaert, O. De Wever, W. Ceelen, Tumour tissue transport after intraperitoneal anticancer drug delivery. *Int. J. Hyperthermia* **33**, 534–542 (2017).
68. A. K. Karayi, V. Basavaraj, S. R. Narahari, M. G. Aggithaya, T. J. Ryan, R. Pilankatta, Human skin fibrosis: Up-regulation of collagen type III gene transcription in the fibrotic skin nodules of lower limb lymphoedema. *Trop. Med. Int. Heal.* **25**, 319–327 (2020).
69. E. B. Dolan, B. Hofmann, M. H. de Vaal, G. Bellavia, S. Straino, L. Kovarova, M. Pravda, V. Velebny, D. Daro, N. Braun, D. S. Monahan, R. E. Levey, H. O'Neill, S. Hinderer, R. Greensmith, M. G. Monaghan, K. Schenke-Layland, P. Dockery, B. P. Murphy, H. M. Kelly, S. Wildhirt, G. P. Duffy, A bioresorbable biomaterial carrier and passive stabilization device to improve heart function post-myocardial infarction. *Mater. Sci. Eng. C Mater. Biol. Appl.* **103**, 109751 (2019).
70. F. B. Coulter, R. E. Levey, S. T. Robinson, E. B. Dolan, S. Deotti, M. Monaghan, P. Dockery, B. S. Coulter, L. P. Burke, A. J. Lowery, R. Beatty, R. Paetzold, J. J. Prendergast, G. Bellavia, S. Straino, F. Cianfarani, M. Salamone, C. M. Bruno, K. M. Moerman, G. Ghersi, G. P. Duffy, E. D. O'Cearbhaill, Additive manufacturing of multi-scale porous soft tissue implants that encourage vascularization and tissue ingrowth. *Adv. Healthc. Mater.* **10**, 2100229 (2021).
71. R. Rezakhaniha, A. Agianniotis, J. T. C. Schrauwen, A. Griffa, D. Sage, C. V. C. Bouten, F. N. Van De Vosse, M. Unser, N. Stergiopulos, Experimental investigation of collagen waviness and orientation in the arterial adventitia using confocal laser scanning microscopy. *Biomech. Model. Mechanobiol.* **11**, 461–473 (2012).
72. RStudio Team, RStudio: Integrated Development for R (RStudio, PBC, 2020); http://rstudio.com/.
73. M. Murbach, B. Gerwe, N. Dawson-Elli, L. Tsui, impedance.py: A Python package for electrochemical impedance analysis. *J. Open Source Softw.* **5**, 2349 (2020).
74. D. Bates, M. Mächler, B. Bolker, S. Walker, Fitting linear mixed-effects models using lme4. *J. Stat. Softw.* **67**, 1–48 (2015).
75. T. Hothorn, K. Hornik, A. Zeileis, ctree: Conditional inference trees. *Compr. R Arch. Netw.*, 1–34 (2015).
76. J. R. Levick, Flow Through interstitium and other fibrous matrices. *Q. J. Exp. Physiol.* **72**, 409–437 (1987).
77. B. S. Gardiner, D. W. Smith, M. Coote, J. G. Crowston, Computational modeling of fluid flow and intra-ocular pressure following glaucoma surgery. *PLOS ONE* **5**, e13178 (2010).
78. M. G. Kenward, J. H. Roger, Small sample inference for fixed effects from restricted maximum likelihood. *Biometrics* **53**, 983–997 (1997).
79. C. Uakarn, K. Chaokromthong, N. Sintao, Sample size estimation using Yamane and Cochran and Krejcie and Morgan and Green formulas and Cohen statistical power analysis by G*power and comparisons. *Apheit Int. J.* **10**, 76–88 (2021).
80. F. Faul, E. Erdfelder, A. Buchner, A. G. Lang, Statistical power analyses using G*Power 3.1: Tests for correlation and regression analyses. *Behav. Res. Methods* **41**, 1149–1160 (2009).

Acknowledgments: We would like to acknowledge the facilities and scientific and technical assistance of the Centre for Microscopy and Imaging at the University of Galway (https://imaging.universityofgalway.ie/imaging/), senior technical officers M. Canney, D. Connolly, and E. McDermott. We also acknowledge the support of the Division of Comparative Medicine (DCM) staff at MIT for the care and postsurgical monitoring of our animals. **Funding:** R.B. and G.P.D. acknowledge funding from Science Foundation Ireland's (SFI) AMBER Centre through their PhD program with grant no. SFI/12/RC/2278. R.B. would like to acknowledge funding from the College of Medicine, Nursing and Health Sciences (CMNHS), University of Galway under a cofunded PhD program with grant no. RSF1591. G.P.D. and L.H.J.S. acknowledge funding from the DELIVER project, which has received funding from the European Union's Horizon 2020 framework program under grant agreement ID 812865. E.T.R., K.L.M., and W.W. acknowledge funding from the Mechanical Engineering Department and the Institute for Medical Engineering and Science at MIT. S.T.R. has received funding from the European Union's Horizon 2020 research and innovation program under the Marie Skłodowska-Curie grant agreement no. 713567. E.B.D. acknowledges funding from the Science Foundation Ireland Royal Society University Research Fellowship (URF\R1\191335). R.T. and J.T. acknowledge funding from SFI's research center for medical devices, CÚRAM, with grant no. 13/RC/2073_P2 and SFI's C2C-GCMP: 19/US-C2C/3633. **Author contributions:** G.P.D., S.T.R., and R.B. conceptualized the work. R.B., K.L.M., W.W., E.B.D., E.T.R., and G.P.D. designed the study. R.B., K.L.M., W.W., L.H.J.S., and J.T. performed the experiments. R.B., L.H.J.S., J.O., P.D., and A.J.S. analyzed and reviewed the data. R.T., L.H.J.S., and Y.F. performed the computational modeling. R.B. and L.H.J.S. wrote the manuscript. All authors reviewed and edited the manuscript. **Competing interests:** E.B.D. is a cofounder and equity holder of Fada Medical. E.T.R is a cofounder of Spheric Bio and Fada Medical, is on the board of directors for Affluent Medical, is on the board of advisers for Pumpinheart and Helios Cardio, and consults for Holistick Medical. G.P.D. is a cofounder, equity holder, and non executive director of Fada Medical and FeelTect Limited. K.L.M., S.T.R., W.W., E.B.D., G.P.D., and E.T.R., alongside S. Rothenbucher and C. Varela, are authors on patent: US20230094196A1—An implantable medical device. **Data and materials availability:** All data needed to evaluate the conclusion in the paper are present in the paper or Supplementary Materials.

Submitted 8 November 2022
Accepted 2 August 2023
Published 30 August 2023
10.1126/scirobotics.abq4821

Science Robotics

Soft robot–mediated autonomous adaptation to fibrotic capsule formation for improved drug delivery

Rachel Beatty, Keegan L. Mendez, Lucien H. J. Schreiber, Ruth Tarpey, William Whyte, Yiling Fan, Scott T. Robinson, Joanne O'Dwyer, Andrew J. Simpkin, Joseph Tannian, Peter Dockery, Eimear B. Dolan, Ellen T. Roche, and Garry P. Duffy

Sci. Robot. **8** (81), eabq4821. DOI: 10.1126/scirobotics.abq4821

Science Robotics (ISSN 2470-9476) is published by the American Association for the Advancement of Science. 1200 New York Avenue NW, Washington, DC 20005. The title *Science Robotics* is a registered trademark of AAAS.